Resolution Dependence of Southern Ocean Mixed-Phase Clouds in ICON

A. Possner*, J. Danker

Institute for Atmospheric and Environmental Sciences, Goethe University Frankfurt, Frankfurt, Germany

E. Gryspeerdt

Faculty of Natural Sciences, The Grantham Institute for Climate Change, London, United Kingdom

**Corresponding author*: Anna Possner, apossner@iau.uni-frankfurt.de

ABSTRACT

Extratropical low-level mixed-phase clouds (MPCs) are difficult to represent in global climate models and generate substantial uncertainty in global climate projections. In this study we evaluate the simulated properties of Southern Ocean (SO) boundary layer MPCs for August 2016 in the ICOsahedral Nonhydrostatic (ICON) model. The bulk of the simulations are part of the DYnamics of the Atmospheric general circulation Modeled On Non-hydrostatic Domain (DYAMOND) initiative.

The analysis shows that previous and current versions of ICON overestimate cloud ice occurrence in low-level clouds across all latitudes in the SO. Furthermore, cloud seeding from upper-level ice clouds into low-level supercooled liquid layers is found to strongly impact MPC occurrence in ICON. Like many other global climate models, ICON underestimates the reflectivity of SO boundary layer clouds. We can show that this effect is resolution dependent and largely due to an underestimation in cloud fraction, rather than optical depth.

Additional sensitivity experiments show a pronounced sensitivity of the Wegener-Bergeron Findeisen (WBF) process with respect to temporal discretisation. Long integration intervals overestimate WBF growth due to the artificially prolonged co-existence of ice and water within the MPC regime. Furthermore, grid-imposed phase homogeneity will likely yield an overestimation in WBF growth rates in simulations performed at the scale of traditional climate models and likely at the convection-permitting scale also. In addition, WBF growth is likely overestimated due to the high bias in low-level cloud ice occurrence. Changes with respect to cloud ice detrainment from shallow convection are of secondary importance for SO MPC statistics.

1. Introduction

In our current climate around 30 % of the Southern Ocean (SO) are covered by low-level stratocumulus and shallow cumulus cloud fields (Wood 2012) reflecting incoming solar radiation and cooling the ocean surface below. Many of these clouds are supercooled at cloud top and often contain not only liquid water, but also ice (Korolev et al. 2017). Simulating these MPCs has posed a considerable challenge for many previous generation and current climate models.

Climate models of the Coupled Model Intercomparison Project phase 5 (CMIP5) experiments considerably underestimated the simulated liquid water content of SO MPCs (McCoy et al. 2015; Bodas-Salcedo et al. 2016b; Tan and Storelvmo 2016; McCoy et al. 2017a) and thus overestimated the shortwave absorption at the surface. This had profound consequences not only for the simulated sea surface temperature in ocean-coupled models (Hyder et al. 2018), but also for regional as well as global estimates in climate sensitivity (Zelinka et al. 2020).

Many CMIP5 models projected a considerable negative cloud feedback due to an extensive cloud-phase feedback by the melting of ice within the MPC under a warming climate. Many new generation models of phase 6 (CMIP6) had corrected their shortwave bias and shortage of simulated liquid water content in SO MPCs. This not only improved model performance in the SO under present-day conditions, but also weakened the simulated cloud feedback in this region, causing an overall increase in global climate sensitivity estimates from CMIP5 to CMIP6 (Zelinka et al. 2020).

MPCs are inherently difficult to capture at full complexity in numerical models across all spatio-temporal scales due to their thermodynamic instability and microphysical complexity. Cloud water is efficiently depleted in the MPC regime through the Wegener-Bergeron-Findeisen (WBF) process (Wegener 1911; Bergeron 1935; Findeisen 1938), where ice crystals grow at the expense of surrounding water droplets due to the lower saturation vapor pressure over ice as compared to water. This process is limited by the spatial coexistence of ice and water in a cloud that statistically contains 100'000 times more droplets than ice crystals. This ratio can be one to two orders of magnitude smaller in regions where secondary ice processes enhance ice crystal number concentrations. Traditionally secondary ice generation through rime splintering (Huang et al. 2017; Young et al. 2019; Lasher-Trapp et al. 2021) or collisional breakup (Sotiropoulou et al. 2021) generally is efficient within convective elements of stratocumulus decks or shallow cumulus clouds. However, our understanding of this process and its occurrence remains limited.

Ultimately, the radiative effect of low-level MPCs is governed by (i) their coverage, (ii) their liquid water content and (iii) their droplet size distribution. Cloud droplets are more efficient at scattering due to their smaller size and higher abundance than ice crystals, which are comparatively negligible in terms of their radiative impact within MPC clouds. Yet, ice formation within MPCs can alter all three of these components, and thus needs to be captured in numerical models assessing the SO cloud feedback or cloud-radiative effect.

In many MPCs the ice and liquid phases are spatially separated, either by vertical separation due to differences in sedimentation speed, or horizontal variability where pockets of ice are found across largely supercooled cloud fields (Korolev et al. 2017). This variability is often poorly represented by coarse-scale climate models. Furthermore, the maintenance of supercooled liquid within MPCs is dependent on sufficiently high updrafts to generate sufficient supersaturation and prevent glaciation through WBF. Once again this relies heavily on model parametrizations of turbulent mixing and shallow convection. Bodas-Salcedo et al. (2019) showed that within the Hadley Centre Global Environmental model (HadGEM3) adjustments in the consideration of turbulent-scale mixing considerably improved their representation of SO MPCs by keeping the supercooled liquid layer alive.

In this study we evaluate the new climate and weather ICOsahedral Nonhydrostatic (ICON) model, which remains largely unverified in the SO with respect to its statistics on SO MPCs and their radiative properties. For these experiments we utilize the DYAMOND (DYnamics of the Atmospheric general circulation Modeled On Non-hydrostatic Domains) runs (Stevens et al. 2020) performed for austral winter where MPC occurrence in the SO is high (Korolev et al. 2017). These simulations were designed to address the uncertainties of the cloud feedback by pushing the climate modelling frontier towards cloud-resolving resolutions (typically referred to the range of mesh sizes of 0.5 – 2 km). The numerical experiments with ICON range from a horizontal resolution of 80 km down to 2.5 km. However, even the highest resolution experiments do not resolve the dynamics of boundary layer cumuli or stratocumuli and only a small fraction of the updraft distribution of deeper cumuli. We thus expect to mainly investigate the impact of spatial and temporal variability on the involved parameterisations under mesoscale synoptic conditions that are either partially resolved (80 km) or fully resolved (2.5 km).

2. Data and methods

A combination of simulations and remote sensing products is used in the following analysis on low-level cloud phase and cloud-radiative properties. A summary of all DYAMOND runs and additional sensitivity experiments is given in Table 1. All remote sensing products are summarised in Table 2.

a. DYAMOND simulations

The bulk of the ICON simulations analysed in this study stem from the DYAMOND initiative (Stevens et al. 2020) conducted for August 2016 in austral winter. The ICON runs performed during this experiment and the involved computational costs are described in detail in Hohenegger et al. (2020) and are downloadable from the Deutsche Klimarechenzentrum (DRKZ). The DYAMOND experiments follow a state-of-the-art configuration of the German Weather Service ("Deutsche Wetterdienst" - DWD) deployed in a limited area setup over the tropical Atlantic (Klocke et al. 2017). Simulations with resolutions coarser than 10 km are performed with and without the Tiedtke-Bechtold mass flux parameterisation (Bechtold et al. 2008; Tiedtke 1989) for deep and shallow convection. The cloud-top height (H_{ct}) and cloud-top temperature (T_{ct}) for low-level clouds with a defined cloud top below 4 km are diagnosed. Thus, we refer to *low-level* clouds to all liquid-containing layers within the column with a defined cloud top below 4 km in both the liquid and ice phase. In this manner the impact of sedimenting ice from upper-level clouds into lower-lying liquid-containing clouds is explicitly excluded for this subset of all clouds. Only time-averaged quantities of qc and qi are stored every 3h. Both variables are used to characterise low-level and overall cloud-phase occurrence rates (F) for all liquid containing clouds. In particular, we distinguish between pure liquid ($F_{liq} = \#liquid/\#[liquid + mixed]$) and mixed-phase ($F_{mix} = \#mixed/\#[liquid + mixed]$) clouds. Different thresholds for qi and qc detection are tested. Unless explicitly stated, the default thresholds of $10^{-4}\,gm^{-3}$ and $10^{-2}\,gm^{-3}$ are applied for qi and qc respectively. The potential impact of: (i) specified thresholds, (ii) use of time-averaged contents, and (iii) the lack of hydrometeor output of snow and graupel within the DYAMOND runs on $F_{liq,mix}$ for the DYAMOND runs is discussed in section 3a.

b. Observations

F_{liq} and F_{mix}, H_{ct} and T_{ct} are compared with active remote sensing retrievals downloaded from the raDAR-liDAR (DARDAR) v2 data product (Delanoë and Hogan 2010; Ceccaldi et al. 2013). This dataset collocates the retrievals from the Cloud-Aerosol Lidar and Infrared Pathfinder Satellite Observations (CALIPSO), CloudSat and analysis fields from the European Centre for Medium-Range Weather Forecasts (ECMWF). Both CALIPSO and CloudSat are part of the afternoon train constellation (L'Ecuyer and Jiang 2010) with an orbiting time of one day. Thus, all latitudes and longitudes with the SO (defined here as between −40°S to −70°S) are sampled. For our analysis we use the generated three-dimensional cloud mask and cloud-phase product along the satellite track.

In order to generate a vertically integrated classification of the overall phase of all liquid-containing clouds, we follow the methodology introduced by Danker et al. (2021). Hereby, different vertically distinct layers of the liquid, mixed and ice categories are combined to a vertically integrated characterisation of either "liquid" or "mixed", which is representative for the entire column. As we are predominantly interested in the shortwave effect of low-level SO clouds, we exclude pure low-level ice clouds from our analysis. We restrict our phase categorisation to the cloud-top region where both lidar and radar retrievals are available. In August 2016 the lidar extinguishes on average within 370 m (interquartile range: 240-420 m). We thus only use simulation output from the first 370 m below cloud top to determine F_{liq} and F_{mix} in all ICON simulations.

Cloud-radiative quantities such as the monthly-mean net top-of-atmosphere (TOA) shortwave flux ($NetTOA_{sw}$) and low (pressure > 680 hPa) cloud fraction (CF_{low}) are evaluated. The Clouds and the Earth's Radiant Energy System (CERES) monthly-mean $NetTOA_{sw}$ is computed from the all-sky shortwave upward and downward fluxes downloaded from https://ceres.larc.nasa.gov/data at one degree spatial resolution (Su et al. 2015). CF_{low} is obtained from the gridded Moderate Resolution Imaging Spectroradiometer (MODIS) level 3 product (https://ladsweb.modaps.eosdis.nasa.gov).

All datasets are remapped bilinearly onto a regular 0.1° by 0.1° which roughly corresponds to a resolution of 10 km in the mid-latitudes. All variables from the DYAMOND simulations, CERES and MODIS retrievals are spatially interpolated onto the 0.1° target grid. For the DARDAR-v2 cloud phase product, a nearest-neighbour approach is chosen.

c. ICON-NWP sensitivity tests

For additional analyses we perform further sensitivity tests with ICON. We use the DWD version 2.6.2 of ICON. The simulations are configured in an identical setting to the DYAMOND ICON experiments with minor updates of which changes in *rat_sea* are most impactful. This namelist parameter specifies the ratio of laminar scaling factors over sea and land and impacts the diagnosed surface fluxes. While changes are observed between model versions, the version update between the DYAMOND runs and the simulations performed in this study do not impact our conclusions. EXP-80-conv is a repetition of DYA-80-conv with additional ice-phase hydrometeor output for snow and graupel (Table 1).

The impact of parametrised convection is assessed within the EXP-80 and EXP-80-convExp simulations. Different models propose different treatments for the detrainment of ice in convective outflows of parameterised convection. Within ICON version 2.6.2 this is treated as follows:

$$
\begin{aligned}
w_{liq} = Min[1.0, 0.25*(T - T_{iceini})] + Min[0, 0.25*(T_{top} - T_{iceini})] \\
QC = QC + w_{liq} * QI_{conv} \\
QI = QI + (1 - w_{liq}) * QI_{conv}
\end{aligned}
\tag{1}
$$

where w_{liq} denotes the fraction of detrained ice which will be converted to liquid, T denotes the temperature at each grid point, $T_{iceini} = 256.15$ is a tuning parameter above which ice is partially detrained as cloud liquid, T_{top} denotes the temperature at the convective cloud top, and QI_{conv} the convective cloud ice at each grid point. Meanwhile, EXP-80 is a repetition of DYA-80 with additional output where all convection parametrisations are turned off (Table 1).

We test the sensitivity to an additional specification of w_{liq} first introduced to reduce the bias in cloud ice in Northern Hemisphere mid-latitude MPCs within the Integrated Forecasting System (IFS) model (Forbes et al. 2016). Here, a more radical approach is taken and $P > 600\,\text{hPa} \implies w_{liq} = 1$. Similar adjustments made within the Community Earth System Model (CESM) improved their SO cloud statistics drastically (Kay et al. 2016).

Finally, we perform two additional simulations investigating the impact of changes in model resolution in ICON version 2.6.2 and in simulations with full ice-phase hydrometeor output. To distinguish the overall sensitivity to model resolution between the two different ICON versions, we repeat the DYA-20-conv simulation in EXP-20-conv using the exact same specifications in addition to EXP-80-conv. The sensitivity with respect to changes in temporal resolution alone are investigated in EXP-80-2.5Dt and EXP-80-20Dt, where time steps of 20 s and 150 s of the 2.5 km and 20 km simulation is prescribed. One final experiment is performed with respect to the terminal fall velocity of ice crystals ($v_{ice,t}$). In EXP-80-Ised $v_{ice,t}$ is reduced from 1.25 ms^{-1} to 0.85 ms^{-1}.

3. Results

a. Threshold impact on cloud phase occurrence rates

Distinguishing between pure liquid clouds and MPCs inherently requires the specification of a threshold of detection for both liquid and ice. In addition, these thresholds may vary across different data products and models, which may inherently bias comparisons across different datasets. This is especially true for the phase characterisation of low-level MPCs, where two phases coincide, but one dominates the other.

It is not the aim and scope of this study to provide a robust uncertainty estimate on cloud-phase retrievals from remote sensing. Yet, we try to establish a feasible uncertainty range estimate from the literature to inform the DARDAR-v2-ICON intercomparison of F_{mix} and F_{liq}. While cloud phase retrievals are widely used, little is known with respect to their quantitative uncertainties, though different sources of errors in cloud-phase detection have been recognised for many years (e.g. Hu et al. 2009; Ceccaldi et al. 2013). Recent work by Villanueva et al. (2021) shows that different remote sensing products may disagree up to 25 % of the time in the SO on the ratio of pure ice with respect to MPCs. In addition, we know that the DARDAR-v2 cloud phase retrievals near cloud top, are likely biased towards the liquid regime, as small ice crystals may escape CloudSat detection.

Within the DYAMOND initiative qc and qi are stored for which detection thresholds have to be specified for the cloud phase categorisation. Here, we investigate the sensitivity to plausible threshold values of liquid and ice ($Min_{qc} = 10^{-2}, 10^{-4}$ gm^{-3} and $Min_{qi} = 10^{-3}, 10^{-4}$ gm^{-3}), as well as the inclusion of additional ice-phase hydrometeor categories such as QS and QG in the computation of F_{liq} and F_{mix}. Fig. 1 shows that small datasets are very susceptible to specified thresholds. This is especially relevant for cloud phase categorisations on the typical timescale of field campaigns. Up to the inclusion of ten thousand data points, choices in threshold and variable impact F_{liq} and F_{mix} estimates up to 125 %.

To quantify this uncertainty we randomly select N points from the daily averaged fields from the EXP-80-conv simulation (i.e. total of 30x3600x300 points in the SO). We repeat this selection 50 times for each N and compute F_{mix} for the three additional threshold specifications listed in Fig. 1. As the dataset increases in size, the relative contribution of low ice water contents vanishes and F_{mix} is thus increasingly less sensitivity to selected minimum cut-off thresholds. However, changing the minimum detectability threshold for q_c generates an uncertainty of 0.1 for F_{mix} and F_{liq}. Decreasing Min_{qc} down to 10^{-4} gm^{-3}, a value far below the detection threshold for in-situ aircraft measurements, shifts the relative occurrence from mixed-phase to liquid clouds by 0.1.

Thus, from the simulations a relatively robust diagnostic for cloud phase occurrence can be generated to within a 0.1 uncertainty range. Meanwhile, the retrieval uncertainty for DARDAR-v2 within the analysed regime remains unquantified, but may be substantial. Remote sensing estimates of F_{mix} (F_{liq}) used in this study should thus be interpreted as a lower (upper) bound on the true relative occurrence rates within supercooled clouds.

b. Resolution dependence of cloud-radiative properties

The DYAMOND experiments provide the unique opportunity to identify and quantify potential biases in simulated SO clouds within ICON across model resolutions ranging from coarse-scale resolutions to convection-permitting scales. The DYA-2.5 simulation alone required 133 million node hours (Hohenegger et al. 2020) to complete at the German Climate Computing Center (DKRZ). Here, we summarise different biases with respect to simulated low-level MPC statistics identified in ICON and discuss their dependence on model resolution.

All DYAMOND experiments parametrising, or partially resolving, convection at the grid-scale are too transparent with respect to incoming solar radiation (Table 3). However, the bias in $\overline{\Delta NetTOA_{sw}}$ (defined here as $+ve$ downward) is reduced by almost a factor 10 from $10.1\,\mathrm{W\,m^{-2}}$ (DYA-80-conv) down to $1.6\,\mathrm{W\,m^{-2}}$ (DYA-2.5) as the spatial resolution increases from 80 km to 2.5 km. Meanwhile, the bias in CF_{low} displays only a very moderate sensitivity with respect to model resolution. The CF_{low} bias is merely reduced by 5 % from DYA-80-conv to DYA-2.5 and CF_{low} remains underestimated by at least 30 % in all simulations. Thus, the increase in cloud reflectance and corresponding decrease in $\overline{\Delta NetTOA_{sw}}$ is caused by an increase in simulated cloud optical depth at higher resolutions.

Regionally, the bias in $\overline{\Delta NetTOA_{sw}}$ (Fig. 3a,b)) is highest at low latitudes where solar insolation is high, the ocean is ice-free (Fig. 3c,d)) and both, liquid and mixed, low-level clouds are common (Fig. 2c)). The strongest reduction in $\Delta NetTOA_{sw}$ with increasing resolution is simulated at low latitudes (Fig. 2a)). Latitudes northward of $-50°$S are characterised by high solar insolation, CF_{low} of at least 60 % (Fig. 2b)), a larger fraction of pure liquid clouds (Fig. 2d)), and a larger LWP_{low} (defined as $LWP\,\forall\,H_{ct} < 4$ km, Fig. 2e)).

The spatial distribution of $\Delta NetTOA_{sw}$ (Fig. 3b)) shows that the reduction in zonal mean $\Delta NetTOA_{sw}$ northward of $-50°$S is largely due to a compensation of errors across regions of moderate biases ranging around $O(\pm 10)\,\mathrm{W\,m^{-2}}$. Regions of pronounced negative biases in shortwave radiation in DYA-2.5 are confined to regions associated with low CF_{low} biases. Similarly $+ve$ biases in $\Delta NetTOA_{sw}$ follow the pattern of underestimated CF_{low}. Similar patterns of $+ve$ and $-ve$ biases in $\Delta NetTOA_{sw}$ (Fig. 3a)) are simulated in DYA-80-conv, although regions of low CF_{low} bias (and Fig. 3c)) are sparse. Thus, all DYAMOND simulations show a "*too few and too bright*" cloud bias (Nam et al. 2012) in SO low-level mid-latitude clouds, which is not uncommon in global climate models (Gettelman et al. 2020). Fig. 3 shows that this bias increases with increasing model resolution, while a compensation of errors improves the domain mean statistic (Table 3).

Additionally, simulated low-level clouds are too bright despite a considerable overestimation of ice occurrence in grid-scale clouds. On average F_{mix} is overestimated by 0.3 (0.25) in all convection-permitting DYA (EXP) runs (Table 3). Unfortunately total ice water content adding up contributions of snow, ice and graupel was not stored for the DYAMOND experiments and can thus not be analysed. We can only speculate that the positive biases in simulated cloud water content and cloud optical depth will likely be enhanced in simulations with corrected low-level cloud phase statistics.

The parameterisation of convection in the coarse-scale DYAMOND runs (DYA-20-conv to DYA-80-conv) acts to decrease cloud cover (Fig. 2b) and LWP_{low} (Fig. 2e)). Both effects result in the change of an overall $+ve$ $NetTOA_{sw}$ radiative mean bias in the SO in simulations with convection to a $-ve$ bias in simulations without a convection parameterisation (Table 3). Within ICON a specified fraction of ice detrained by the convection scheme is detrained as cloud water following equ. 1. An alternative parametrisation improving MPC biases within the IFS was tested in EXP-80-convExp. In this experiment all convective cloud ice is assumed to be detrained as liquid below 680 hPa in altitude. However, while this greatly improved the representation of supercooled cloud water within the IFS model, LWP_{low} and IWP_{low} remain virtually unaffected by this change.

c. Resolution dependence of cloud phase

MPC observations show a large amount of spatial variability in ice occurrence, which is missed in ICON. The model also does not capture the large-scale gradients in low-level MPC occurrence. Observed latitudinal gradients in F_{mix} (F_{liq}) display a distinct mountain (valley) shaped curve (Fig. 2c,d)). F_{mix} initially doubles from 31 % at −40° S to 62 % at −57° S before dropping down to 1 % at high latitudes (Fig. 2c)). This pattern has been previously observed in space-born remote sensing observations (Gryspeerdt et al. 2018; Mace et al. 2021; Lang et al. 2021) and was linked to enhanced low-level cloud occurrence in the cold sectors of cyclones (Fletcher et al. 2016) and marine cold air outbreaks (McCoy et al. 2017b). During August 2016 the sea ice fraction decreases from 90 % to 0 % between −70° S to −55° S, pushing the SO storm track and marine cold air outbreak activity northward as compared to austral summer. The mean latitude of the Antarctic polar front is identified at −60° S by searching the southernmost gradient in SST exceeding 1.5° C km^{-1} (Freeman and Lovenduski 2016). Regions north of the polar front are associated with higher cyclonic activity and larger surface fluxes. Both of which result in more mixing and thus potentially low-level clouds with higher updrafts that sustain ice formation or enhance cloud ice concentrations through secondary ice generation. Its location corresponds to the onset of F_{mix} decline in the observations, which is consistent with results from Mace et al. (2021), where only the CALIPSO cloud lidar was used for phase identification. Meanwhile, Listowski et al. (2019) hypothesises that limitations of biogenic ice nucleating particles from sea spray emissions by increasing sea ice cover may cause the latitudinal decline in F_{mix}.

While all studies from different time periods, using different analysis methods, observe this drop-off in F_{mix} with increasing latitude (Listowski et al. 2019; Mace et al. 2021; Lang et al. 2021), a complete causal explanation of this association is still lacking. Meanwhile, all simulations (independent of model resolution) capture the increase in F_{mix} at low latitudes (though they overestimate F_{mix} by at least 20 %). However, not one simulation captures the drop off in F_{mix} at high latitudes. All ICON versions considered for this study do not include a prognostic treatment of INP and would thus not be expected to capture effects of INP limitations. However, the absence of the decline in F_{mix} at high latitudes in combination with the general overestimation of F_{mix} across all latitudes (Fig. 2c), T_{ct} (Fig. 4a)) and H_{ct} (Fig. 4b)) ranges, suggest that ICON generally overestimates the presence of ice in low supercooled SO clouds.

F_{mix} and F_{liq} show some variability with respect to model resolution at low latitudes (Fig. 2c)) characterised by warmer temperatures ($\overline{T_{ct}} > -10\,°C$) and intermediate heights (1 km$< H_{ct} <$ 2.5 km). This variability is caused by changes in seeding frequency (F_{seed}) where ice sediments from above into the supercooled layer. For example F_{seed} drops from 20 % to 11 % and F_{mix} decreases by 22 % (absolute value) as model resolution increases from 80 km to 2.5at $-41°$S. Towards $-55°$ differences in F_{seed} across resolutions decrease and F_{mix} approaches the limit of 1.0. The resolution dependence of F_{seed} is somewhat surprising, as all grid points entering the above statistics have been filtered to remove all upper-level cloud above the liquid cloud top for comparability to the DARDAR-v2 statistics, which apply the same filter. This suggests, that these clouds had been seeded previously in their history and that this process occurs often enough to impact domain mean cloud statistics. Low-level MPCs can be maintained for days (Morrison et al. 2012) and recycling of INP has been shown to contribute to their longevity (Solomon et al. 2015). Furthermore, low cloud formation in the SO generally is found in the wake of deeper convection (mesoscale and large-scale fronts). It is thus not inconceivable that remnants of upper level convection and mid-level ice clouds seed supercooled boundary layer clouds below. However, to the authors knowledge little is known about the seeding frequency of low-level clouds in the SO. These simulations suggest that seeding may play an important role, but these results remain to be verified in future studies.

d. Impact of spatial versus temporal resolution

The additional sensitivity runs performed with ICON version 2.6.2 allow us to investigate the sensitivity of MPC properties with respect to spatial and temporal resolution separately, while also storing complete ice-phase hydrometeor output. Code developments and namelist adjustments between the different model versions already contribute to a reduction of the radiative bias at coarse resolutions (Table 3). However, already at 20 km spatial resolution the bias reduction in $\Delta NetTOA_{sw}$ is decreased by 34,% as compared to the 80 km experiments. H_{ct} and F_{mix} statistics are also improved (Table 3) in the newer ICON version as compared to DARDAR-v2 observations. Thus, results between the model versions are not directly transferable. However, their overall changes with spatio-temporal resolution and overall bias structures are unaffected by the many changes made between the two model versions.

The cross sections in Fig. 5a) show two distinct simulated growth modes of cloud ice in the SO, which is dominated by the snow category (average mass fraction of 70%): (i) a pure depositional (DEP) growth mode which peaks at the surface south of −65°S over the Antarctic ice sheet (sea ice fraction > 80 %) , and (ii) a WBF growth mode within the liquid cloud layer and subsequent melting or sublimation north of ∼ −63°S.

Both ice growth mechanisms show a distinct and opposite dependence on temporal resolution. Fig. 5 shows the additional cross sections for EXP-80-conv-20Dt (Fig. 5b)), where only temporal resolution is increased. We simulate larger increases in QI_{tot} towards the surface above the Antarctic ice sheet. This is indicative of enhanced DEP growth in this region at smaller time steps. Meanwhile, further north maximum QI_{tot} concentrations are simulated within the supercooled liquid layer. We argue that simulations with coarse time steps (up to 6.5 min in this study) overestimate the residence time of ice crystals within this layer, which leads to excessive WBF growth. In reality WBF growth, while efficient, is a somewhat self-limiting process due to the depletion of cloud water within the ice crystals vicinity. The resulting gradients between ice and water slow further growth of the ice crystals. This variability is not captured in these simulations which assume homogeneous mixing at the grid scale. Thus, an overestimation of incloud residence times of ice crystals has a tremendous impact on simulated WBF growth.

A further increase in time step from 2.5 min to 20 s (EXP-80-2.5Dt) leads to a further, but more moderate, reduction in simulated QI_{tot} (not shown) and in IWP_{low} from 57 g m^{-2} (EXP-80-20Dt) to 53 g m^{-2} (EXP-80-2.5Dt) north of −63°S. In EXP-80-conv IWP_{low} is diagnosed as 68 g m^{-2} in the WBF growth region. Meanwhile, only a moderate sensitivity with respect to $v_{ice,t}$ was found in the WBF growth region. Once again reemphasising the time-step dependence within this regime. Decreasing this tuning parameter by 32% in EXP-80-conv-Ised increases IWP_{low} by merely 1 g m^{-2} north of −63°S. At the same time, a stronger increase in IWP_{low} is simulated over the Antarctic ice sheet where DEP growth rates dominate. Here, IWP_{low} increases from 114 g m^{-2} to 130 g m^{-2}.

An increase in spatial resolution is not found to impact DEP rates above the Antarctic ice sheet ((Fig. 5c)). Yet, both qc_{tot} and QI_{tot} increase within the WBF growth region. This combined increase in ice and liquid within the mixed-phase regime suggests a simultaneous increase in simulated supersaturation with respect to ice and liquid at finer resolutions. Given that the majority of all grid points containing boundary layer clouds are mixed phase, we do not expect horizontal resolution to impact cloud phase variability in the simulations shown here. In the absence of differences in atmospheric moisture content (not shown), T_{ct} or H_{ct} (Table 3), we suspect the increased levels of supersaturation to be sustained by increased mixing diagnosed over smaller horizontal scales.

The combined impact of spatial and horizontal resolution changes is summarised in Fig. 6. We find the percentage change in LWP_{low} by time step and spatial resolution to be almost additive. Both, decreased WBF growth (time step sensitivity) and increased supersaturations (spatial resolution sensitivity) contribute to the overall increase in simulated LWP_{low}. Meanwhile, opposing effects due to quicker sedimentation through WBF growth regions (time step sensitivity) and increased supersaturations (spatial resolution sensitivity) compensate, which yields a negligible change in simulated IWP_{low} as the model resolution is increased.

4. Discussion

The results of this study indicate that the DWD version of ICON overestimates the occurrence of low-level MPCs, while underestimating cloud fraction, and the shortwave cloud-radiative effect. Thus, like many other CMIP5 models (Zelinka et al. 2020), this version will likely overestimate climate sensitivity in this region due to an excessive cloud-phase feedback in a warmer climate (Bodas-Salcedo et al. 2016b,a). We could further identify future research avenues to overcome these shortcomings. For one, all ICON simulations display a distinct pattern of the common "*too-few, but too-bright*" bias. Future tests exploring the treatment of cloud cover and cloud water entering the radiation scheme in ICON, may be able to reduce these determined biases.

Secondly, we show that the growth mechanisms of ice in the mixed-phase regime (WBF growth) and the DEP growth regime are resolution dependent. However, we suspect that the largest bias in resolution is currently hidden by the general overestimation in ice occurrence within supercooled liquid SO clouds. WBF growth rates are conditional on the spatial coexistence of ice and liquid within the same cloud volume. The spatial heterogeneity of phase variability in boundary-layer MPCs remains poorly constrained, which is largely due to the absence of consistent observations from spatial scales of a few metres to several kilometres over long time periods. Ruiz-Donoso et al. (2020) showed that scales of cloud phase variability may be on the order of tens of meters. Here, we analyse the phase variability on the mesoscale by analysing phase variability along the combined CALIPSO-CLOUDSAT footprint (~ 1.1 km). Fig. 7 shows the percentage of mixed-phase points along all identified continuous liquid-containing cloud segments of length Δx. Already a doubling in Δx from the footprint to 2.5 km shows that these segments on average consist of 83 % mixed-phase and 17% liquid phase DARDAR-v2 footprints. Meanwhile, one single cloud phase (in this case liquid or mixed) is diagnosed over the entirety of a grid box of size Δx. Along an 80 km segment which would be classified as mixed-phase, merely 18 % of all 1.1 km cloud segments contain ice and are surrounded by pixels containing pure supercooled liquid. Thus, climate models with large grid mesh sizes are likely to significantly overestimate WBF growth rates if one does not account for the artificial phase homogenisation in the absence of sub-gridscale phase variability. Furthermore, the drop in $F_{liq+ice}$ (see caption Fig. 7) from DADAR-v2 footprint size to 2.5 km suggests that the true characteristic scale of cloud phase variability resides in the sub-kilometre range. Thus, we speculate that representation of sugbrid-scale phase variability are also required in climate simulations performed at the convection-permitting scale. Finally, the general overestimation of MPC occurrence in these simulations merits further investigation. Both ICON versions show a strong sensitivity of the low-latitude cloud phase (F_{mix}) to the seeding frequency from mid- or upper troposphere clouds (F_{seed}). At least 20 % of all MPCs in convection-permitting simulations at any given time are in direct contact with cloud ice above the liquid cloud top. Furthermore, our results show that cloud statistics from boundary layer clouds which are filtered for clear-sky free-tropospheric conditions, are affected by seeding in their past. Meanwhile, the direct verification of this process from observations remains difficult. Few long-term remote sensing or atmospheric profiling statistics investigating multi-layer low- and mid-level cloud systems exist over the SO.

The few that do exist are insufficient to evaluate these simulations directly, but confirm that this process may play a significant role. Ground-based remote sensing observations near East Antarctica provide evidence for several seeding events of single-layer supercooled liquid clouds trailing strong precipitation events (Alexander et al. 2021). The recent climatology compiled of vertical profiles across four different field campaigns also suggests that multi-level clouds occur frequently in the vicinity of fronts and cyclone activity (Truong et al. 2020). Thus, the importance of upper level cloud seeding suggested in these simulations remains to be explored in future studies.

5. Conclusions

We use the DYAMOND ICON DWD experiments for August 2016 to evaluate ICON during austral winter over the SO ($-40°S - -70°S$). Many climate models are prone to substantial biases in $NetTOA_{sw}$ due to biased representations of supercooled liquid low-level clouds, or MPCs, over the SO. The main conclusions of this study are summarised as follows:

- MPC occurrence is overestimated by 30% on average in all convection-permitting or convection-parametrising simulations as compared to DARDAR-v2 cloud phase statistics.

- WBF growth is strongly time step dependent due to reduced ice sedimentation at coarse integration intervals and an artificially prolonged co-existence of liquid and ice within MPCs.

- DEP growth rates over the Antarctic ice sheet are impacted by time step and the namelist parameter for the terminal fall velocity of ice ($v_{ice,t}$). Both impact ice residence times in supercooled environments with respect to ice, and thus DEP growth rates.

- Upper-level cloud seeding into boundary layer supercooled liquid clouds is found to govern low-latitude SO cloud phase and supercooled water content in ICON.

- While the monthly mean spatial pattern of cloudiness is captured as compared to MODIS observations, cloud fraction and $NetTOA_{sw}$ are strongly underestimated.

- Monthly mean net TOA short-wave bias decreases from 10 W m^{-2} to 1.6 W m^{-2} for simulations performed at the cloud-resolving scale. However, considerable biases in SO climate sensitivity due to an excessive cloud-phase feedback is still expected for climate simulations at the convection-permitting scale due to the overestimation of MPC occurrence.

Acknowledgments. DYAMOND data management was provided by the German Climate Computing Center (DKRZ) and supported through the projects ESiWACE and ESiWACE2. The projects ESiWACE and ESiWACE2 have received funding from the European Union's Horizon 2020 research and innovation programme under grant agreements No 675191 and 823988. This work used resources of the Deutsches Klimarechenzentrum (DKRZ) granted by its Scientific Steering Committee (WLA) under project IDs bk1040, bb1153 and bb1137.

We would like to acknowledge personal contributions from Dr. Daniel Klocke for his shared insights into the DYAMOND experiments, Dr. Odran Sourdeval for access to the DARDAR-v2 archives. Kevin Pfannkuch for his contribution to plot scripting. A. Possner and J. Danker were funded by the Federal Ministry of Education and Research (BMBF) under the "Make our Planet Great Again – German Research Initiative", grant number 57429624, implemented by the German

Academic Exchange Service (DAAD). E. Gryspeerdt was supported by a Royal Society University Research Fellowship (URF/R1/191602).

Data availability statement. The DARDAR-MASK v2.23 products are available on the Aeris/ICARE data center (http://www.icare.univ-lille1.fr/, last access: August 2021). CERES fluxes are downloaded from `https://ceres.larc.nasa.gov/data` (last access: December 2021) at one degree spatial resolution and MODIS level 3 retrievals from `https://ladsweb.modaps.eosdis.nasa.gov` (last access: December 2021). All DYAMOND output fields and simulation protocols can be obtained by following the data access instructions published here: `https://www.esiwace.eu/services/dyamond-initiative` (last access: January 2021). A complete description of all data sets used in this study is provided in sections 2a, 2b and 2c.

References

Alexander, S. P., G. M. McFarquhar, R. Marchand, A. Protat, Vignon, G. G. Mace, and A. R. Klekociuk, 2021: Mixed-phase clouds and precipitation in southern ocean cyclones and cloud systems observed poleward of 64°s by ship-based cloud radar and lidar. *Journal of Geophysical Research: Atmospheres*, **126 (8)**, e2020JD033 626, doi: https://doi.org/10.1029/2020JD033626, URL https://agupubs.onlinelibrary.wiley.com/doi/abs/10.1029/2020JD033626, e2020JD033626 2020JD033626, https://agupubs.onlinelibrary.wiley.com/doi/pdf/10.1029/2020JD033626.

Bechtold, P., M. Köhler, T. Jung, F. Doblas-Reyes, M. Leutbecher, M. J. Rodwell, F. Vitart, and G. Balsamo, 2008: Advances in simulating atmospheric variability with the ecmwf model: From synoptic to decadal time-scales. *Quarterly Journal of the Royal Meteorological Society*, **134 (634)**, 1337–1351, doi:https://doi.org/10.1002/qj.289, URL https://rmets.

onlinelibrary.wiley.com/doi/abs/10.1002/qj.289, https://rmets.onlinelibrary.wiley.com/doi/pdf/10.1002/qj.289.

Bergeron, T., 1935: *On the physics of clouds and precipitation*. in *Proces Verbaux de l'Association de Mètèorologie, 5th asssembly of the International Union of geodesy and geophysics* ed., Paul Dupont, Paris, France, 156–178 pp.

Bodas-Salcedo, A., T. Andrews, A. V. Karmalkar, and M. A. Ringer, 2016a: Cloud liquid water path and radiative feedbacks over the southern ocean. *Geophysical Research Letters*, **43 (20)**, 10,938–10,946, doi:https://doi.org/10.1002/2016GL070770, URL https://agupubs.onlinelibrary.wiley.com/doi/abs/10.1002/2016GL070770, https://agupubs.onlinelibrary.wiley.com/doi/pdf/10.1002/2016GL070770.

Bodas-Salcedo, A., P. G. Hill, K. Furtado, K. D. Williams, P. R. Field, J. C. Manners, P. Hyder, and S. Kato, 2016b: Large contribution of supercooled liquid clouds to the solar radiation budget of the southern ocean. *Journal of Climate*, **29 (11)**, 4213 – 4228, doi:10.1175/JCLI-D-15-0564.1, URL https://journals.ametsoc.org/view/journals/clim/29/11/jcli-d-15-0564.1.xml.

Bodas-Salcedo, A., J. P. Mulcahy, T. Andrews, K. D. Williams, M. A. Ringer, P. R. Field, and G. S. Elsaesser, 2019: Strong dependence of atmospheric feedbacks on mixed-phase microphysics and aerosol-cloud interactions in hadgem3. *Journal of Advances in Modeling Earth Systems*, **11 (6)**, 1735–1758, doi:https://doi.org/10.1029/2019MS001688, URL https://agupubs.onlinelibrary.wiley.com/doi/abs/10.1029/2019MS001688, https://agupubs.onlinelibrary.wiley.com/doi/pdf/10.1029/2019MS001688.

Ceccaldi, M., J. Delanoë, R. J. Hogan, N. L. Pounder, A. Protat, and J. Pelon, 2013: From CloudSat-CALIPSO to EarthCare: Evolution of the DARDAR cloud classification and its comparison to airborne radar-lidar observations. *Journal of Geophysical Research Atmospheres*, **118 (14)**, 7962–7981, doi:10.1002/jgrd.50579.

Danker, J., O. Sourdeval, I. L. McCoy, R. Wood, and A. Possner, 2021: Exploring relations between cloud morphology, cloud phase, and cloud radiative properties in southern ocean stratocumulus clouds. *Atmospheric Chemistry and Physics Discussions*, **2021**, 1–26, doi:10.5194/acp-2021-926, URL https://acp.copernicus.org/preprints/acp-2021-926/.

Delanoë, J., and R. J. Hogan, 2010: Combined CloudSat-CALIPSO-MODIS retrievals of the properties of ice clouds. *Journal of Geophysical Research Atmospheres*, **115 (4)**, doi:10.1029/2009JD012346.

Findeisen, W., 1938: Kolloid-meteorologische vorgänge bei niederschlagsbildung. *Meteorol. Z.*, **55**, 121–133.

Fletcher, J. K., S. Mason, and C. Jakob, 2016: A climatology of clouds in marine cold air outbreaks in both hemispheres. *Journal of Climate*, **29 (18)**, 6677 – 6692, doi:10.1175/JCLI-D-15-0783.1, URL https://journals.ametsoc.org/view/journals/clim/29/18/jcli-d-15-0783.1.xml.

Forbes, R., A. J. Geer, K. Lonitz, and M. Ahlgrimm, 2016: Reducing systematic errors in cold-air outbreaks. 17–22, doi:10.21957/s41h7q7l, URL https://www.ecmwf.int/node/17261.

Freeman, N. M., and N. S. Lovenduski, 2016: Mapping the antarctic polar front: weekly realizations from 2002 to 2014. *Earth System Science Data*, **8 (1)**, 191–198, doi:10.5194/essd-8-191-2016, URL https://essd.copernicus.org/articles/8/191/2016/.

Gettelman, A., and Coauthors, 2020: Simulating observations of southern ocean clouds and implications for climate. *Journal of Geophysical Research: Atmospheres*, **125 (21)**, e2020JD032 619, doi:https://doi.org/10.1029/2020JD032619, URL https://agupubs.onlinelibrary.wiley.com/doi/

abs/10.1029/2020JD032619, e2020JD032619 10.1029/2020JD032619, https://agupubs.onlinelibrary.wiley.com/doi/pdf/10.1029/2020JD032619.

Gryspeerdt, E., O. Sourdeval, J. Quaas, J. Delanoë, M. Krämer, and P. Kühne, 2018: Ice crystal number concentration estimates from lidar–radar satellite remote sensing – part 2: Controls on the ice crystal number concentration. *Atmospheric Chemistry and Physics*, **18 (19)**, 14 351–14 370, doi:10.5194/acp-18-14351-2018, URL https://acp.copernicus.org/articles/18/14351/2018/.

Hohenegger, C., L. Kornblueh, D. Klocke, T. Becker, G. Cioni, J. F. Engels, U. Schulzweida, and B. Stevens, 2020: Climate statistics in global simulations of the atmosphere from 80 to 2.5 km grid spacing. *Journal of the Meteorological Society of Japan*, **98**, 73 – 91, doi: 10.2151/jmsj.2020-005.

Hu, Y., and Coauthors, 2009: Calipso/caliop cloud phase discrimination algorithm. *Journal of Atmospheric and Oceanic Technology*, **26 (11)**, 2293 – 2309, doi:10.1175/2009JTECHA1280.1, URL https://journals.ametsoc.org/view/journals/atot/26/11/2009jtecha1280_1.xml.

Huang, Y., T. Chubb, D. Baumgardner, M. deHoog, S. T. Siems, and M. J. Manton, 2017: Evidence for secondary ice production in southern ocean open cellular convection. *Quarterly Journal of the Royal Meteorological Society*, **143 (704)**, 1685–1703, doi:https://doi.org/10.1002/qj.3041, URL https://rmets.onlinelibrary.wiley.com/doi/abs/10.1002/qj.3041, https://rmets.onlinelibrary.wiley.com/doi/pdf/10.1002/qj.3041.

Hyder, P., and Coauthors, 2018: Critical southern ocean climate model biases traced to atmospheric model cloud errors. *Nat Commun*, **9 (3625)**, doi:10.1038/s41467-018-05634-2.

Kay, J. E., C. Wall, V. Yettella, B. Medeiros, C. Hannay, P. Caldwell, and C. Bitz, 2016: Global climate impacts of fixing the southern ocean shortwave radiation bias in the community earth system model (cesm). *Journal of Climate*, **29 (12)**, 4617 – 4636, doi:10.1175/JCLI-D-15-0358.1, URL https://journals.ametsoc.org/view/journals/clim/29/12/jcli-d-15-0358.1.xml.

Klocke, D., M. Brueck, C. Hohenegger, and B. Stevens, 2017: Rediscovery of the doldrums in storm-resolving simulations over the tropical atlantic. *Nature Geosci*, **10**, 891—-896, doi: 10.1038/s41561-017-0005-4.

Korolev, A., and Coauthors, 2017: Mixed-Phase Clouds: Progress and Challenges. *Meteorological Monographs*, **58**, 5.1–5.50, doi:10.1175/AMSMONOGRAPHS-D-17-0001.1.

Lang, F., L. Ackermann, Y. Huang, S. C. H. Truong, S. T. Siems, and M. J. Manton, 2021: A climatology of open and closed mesoscale cellular convection over the southern ocean derived from himawari-8 observations. *Atmospheric Chemistry and Physics Discussions*, **2021**, 1–27, doi:10.5194/acp-2021-681, URL https://acp.copernicus.org/preprints/acp-2021-681/.

Lasher-Trapp, S., E. L. Scott, E. Järvinen, M. Schnaiter, F. Waitz, P. J. DeMott, C. S. McCluskey, and T. C. J. Hill, 2021: Observations and modeling of rime splintering in southern ocean cumuli. *Journal of Geophysical Research: Atmospheres*, **126 (23)**, e2021JD035 479, doi: https://doi.org/10.1029/2021JD035479, URL https://agupubs.onlinelibrary.wiley.com/doi/abs/10.1029/2021JD035479, e2021JD035479 2021JD035479, https://agupubs.onlinelibrary.wiley.com/doi/pdf/10.1029/2021JD035479.

Listowski, C., J. Delanoë, A. Kirchgaessner, T. Lachlan-Cope, and J. King, 2019: Antarctic clouds, supercooled liquid water and mixed phase, investigated with dardar: geographical and seasonal variations. *Atmospheric Chemistry and Physics*, **19 (10)**, 6771–6808, doi:10.5194/acp-19-6771-2019, URL https://acp.copernicus.org/articles/19/6771/2019/.

L'Ecuyer, T. S., and J. H. Jiang, 2010: Touring the atmosphere aboard the a-train. *Physics Today*, **63 (7)**, 36–41, doi:10.1063/1.3463626, URL https://doi.org/10.1063/1.3463626.

Mace, G. G., A. Protat, and S. Benson, 2021: Mixed-phase clouds over the southern ocean as observed from satellite and surface based lidar and radar. *Journal of Geophysical Research: Atmospheres*, **126 (16)**, e2021JD034 569, doi:https://doi.org/10.1029/2021JD034569, URL https://agupubs.onlinelibrary.wiley.com/doi/abs/10.1029/2021JD034569, e2021JD034569 2021JD034569, https://agupubs.onlinelibrary.wiley.com/doi/pdf/10.1029/2021JD034569.

McCoy, D. T., F. A.-M. Bender, J. K. C. Mohrmann, D. L. Hartmann, R. Wood, and D. P. Grosvenor, 2017a: The global aerosol-cloud first indirect effect estimated using MODIS, MERRA, and AeroCom. *Journal of Geophysical Research: Atmospheres*, **122 (3)**, 1779–1796, doi:10.1002/2016JD026141, URL https://agupubs.onlinelibrary.wiley.com/doi/abs/10.1002/2016JD026141, https://agupubs.onlinelibrary.wiley.com/doi/pdf/10.1002/2016JD026141.

McCoy, D. T., D. L. Hartmann, M. D. Zelinka, P. Ceppi, and D. P. Grosvenor, 2015: Mixed-phase cloud physics and southern ocean cloud feedback in climate models. *Journal of Geophysical Research: Atmospheres*, **120 (18)**, 9539–9554, doi:https://doi.org/10.1002/2015JD023603, URL https://agupubs.onlinelibrary.wiley.com/doi/abs/10.1002/2015JD023603, https://agupubs.onlinelibrary.wiley.com/doi/pdf/10.1002/2015JD023603.

McCoy, I. L., R. Wood, and J. K. Fletcher, 2017b: Identifying meteorological controls on open and closed mesoscale cellular convection associated with marine cold air outbreaks. *Journal of Geophysical Research: Atmospheres*, **122 (21)**, 11,678–11,702, doi:10.1002/2017JD027031, URL http://dx.doi.org/10.1002/2017JD027031, 2017JD027031.

Morrison, H., G. de Boer, G. Feingold, J. Harrington, M. D. Shupe, and K. Sulia, 2012: Resilience of persistent Arctic mixed-phase clouds. *Nature Geoscience*, **5**, 11–17, doi:10.1038/ngeo1332.

Nam, C., S. Bony, J.-L. Dufresne, and H. Chepfer, 2012: The 'too few, too bright' tropical low-cloud problem in CMIP5 models. *Geophys. Res. Lett.*, **39**, L21 801, doi:10.1029/2012GL053421.

Ruiz-Donoso, E., and Coauthors, 2020: Small-scale structure of thermodynamic phase in arctic mixed-phase clouds observed by airborne remote sensing during a cold air outbreak and a warm air advection event. *Atmospheric Chemistry and Physics*, **20 (9)**, 5487–5511, doi:10.5194/acp-20-5487-2020, URL https://acp.copernicus.org/articles/20/5487/2020/.

Solomon, A., G. Feingold, and M. D. Shupe, 2015: The role of ice nuclei recycling in the maintenance of cloud ice in Arctic mixed-phase stratocumlus. *Atmos. Chem. Phys.*, **15**, 10 631–10 643.

Sotiropoulou, G., E. Vignon, G. Young, H. Morrison, S. J. O'Shea, T. Lachlan-Cope, A. Berne, and A. Nenes, 2021: Secondary ice production in summer clouds over the antarctic coast: an underappreciated process in atmospheric models. *Atmospheric Chemistry and Physics*, **21 (2)**, 755–771, doi:10.5194/acp-21-755-2021, URL https://acp.copernicus.org/articles/21/755/2021/.

Stevens, B., and Coauthors, 2020: The added value of large-eddy and storm-resolving models for simulating clouds and precipitation. *Journal of the Meteorological Society of Japan. Ser. II*, **98 (2)**, 395–435, doi:10.2151/jmsj.2020-021.

Su, W., J. Corbett, Z. Eitzen, and L. Liang, 2015: Next-generation angular distribution models for top-of-atmosphere radiative flux calculation from ceres instruments: methodology. *Atmospheric Measurement Techniques*, **8 (2)**, 611–632, doi:10.5194/amt-8-611-2015, URL https://amt.copernicus.org/articles/8/611/2015/.

Tan, I., and T. Storelvmo, 2016: Sensitivity study on the influence of cloud microphysical parameters on mixed-phase cloud thermodynamic phase partitioning in cam5. *Journal of the Atmospheric Sciences*, **73 (2)**, 709 – 728, doi:10.1175/JAS-D-15-0152.1, URL https://journals.ametsoc.org/view/journals/atsc/73/2/jas-d-15-0152.1.xml.

Tiedtke, M., 1989: A comprehensive mass flux scheme for cumulus parameterization in large-scale models. *Quart. J. Roy. Meteor. Soc.*, **117**, 1779–1800.

Truong, S. C. H., Y. Huang, F. Lang, M. Messmer, I. Simmonds, S. T. Siems, and M. J. Manton, 2020: A climatology of the marine atmospheric boundary layer over the southern ocean from four field campaigns during 2016–2018. *Journal of Geophysical Research: Atmospheres*, **125 (20)**, e2020JD033 214, doi:https://doi.org/10.1029/2020JD033214, URL https://agupubs.onlinelibrary.wiley.com/doi/abs/10.1029/2020JD033214, e2020JD033214 2020JD033214, https://agupubs.onlinelibrary.wiley.com/doi/pdf/10.1029/2020JD033214.

Villanueva, D., F. Senf, and I. Tegen, 2021: Hemispheric and seasonal contrast in cloud thermodynamic phase from a-train spaceborne instruments. *Journal of Geophysical Research: Atmospheres*, **126 (6)**, e2020JD034 322, doi:https://doi.org/10.1029/2020JD034322, URL https://agupubs.onlinelibrary.wiley.com/doi/abs/10.1029/2020JD034322, e2020JD034322 2020JD034322, https://agupubs.onlinelibrary.wiley.com/doi/pdf/10.1029/2020JD034322.

Wegener, A., 1911: *Thermodynamik der Atmosphäre*. Leipzig, J. A. Barth, 1911.

Wood, R., 2012: Review: Stratocumulus clouds. *Mon. Wea. Rev.*, **140**, 2373–2423.

Young, G., T. Lachlan-Cope, S. J. O'Shea, C. Dearden, C. Listowski, K. N. Bower, T. W. Choularton, and M. W. Gallagher, 2019: Radiative effects of secondary ice enhancement in coastal antarctic clouds. *Geophysical Research Letters*, **46 (4)**, 2312–2321, doi:https://doi.org/10.1029/2018GL080551, URL https://agupubs.onlinelibrary.wiley.com/doi/abs/10.1029/2018GL080551, https://agupubs.onlinelibrary.wiley.com/doi/pdf/10.1029/2018GL080551.

Zelinka, M. D., T. A. Myers, D. T. McCoy, S. Po-Chedley, P. M. Caldwell, P. Ceppi, S. A. Klein, and K. E. Taylor, 2020: Causes of higher climate sensitivity in cmip6 models. *Geophysical Research Letters*, **47 (1)**, e2019GL085 782, doi:https://doi.org/10.1029/2019GL085782, URL https://agupubs.onlinelibrary.wiley.com/doi/abs/10.1029/2019GL085782, e2019GL085782 10.1029/2019GL085782, https://agupubs.onlinelibrary.wiley.com/doi/pdf/10.1029/2019GL085782.

LIST OF TABLES

[1] [*above open ocean only]

TABLE 1. Overview of all DYAMOND runs for August 2016 used in this study. The following variables stand for: qc=time-averaged cloud water content, qi=time-averaged ice water content, QC=instantaneous cloud water content, QI=instantaneous cloud ice content, QS=instantaneous snow content, QG=instantaneous graupel content, H_{ct}=cloud-top height, T_{ct}=cloud-top temperature, P_{ct}=cloud-top pressure, and CF=low-level cloud fraction (i.e. pressure > 680 hPa). All additional ICON experiments were performed with a newer ICON version (2.6.2).

DYAMOND ICON runs			
acronym	resolution [km / s]	variables	Comments
DYA-80-conv	80/450	qc, qi, H_{ct}, T_{ct}, P_{ct}, CF_{low}, NetTOA$_{sw}$	
DYA-80			no conv
DYA-40-conv	40/225		
DYA-40			no conv
DYA-20-conv	20/150		
DYA-20			no conv
DYA-10	10/90		
DYA-5	5/45		
DYA-2.5	2.5/20		
Additional ICON Experiments			
EXP-80	80/450	qc, qi, QC, QI, QS, QG, H_{ct}, T_{ct}, P_{ct}, CF_{low}, $NetTOA_{sw}$	as DYA-80
EXP-80-conv			as DYA-80-conv
EXP-80-convExp			all detrained cloud ice >600 hPa converted to liquid
EXP-20-conv	20/150		as DYA-20-conv
EXP-80-20Dt	80/150		using Exp-20 time step
EXP-80-2.5Dt	80/20		using DYA-2.5 time step
EXP-80-Ised	80/450		ice terminal fall velocity = 0.85 m s^{-1} (default 1.25)

TABLE 2. Summary of remote sensing products used in this study.

Remote Sensing Products		
acronym	resolution [space/time]	variables
DARDAR-v2	1.1 km / <1day	F_{liquid},F_{mixed},H_{ct},T_{ct}
CERES	1°/monthly	NetTOA$_{sw}$
MODIS	1°/monthly	CF_{low}

[2][*above open ocean only]

TABLE 3. Summary table of SO cloud properties and radiative fluxes.[2]

datatype	$\overline{NetTOA_{sw}}$ [W m^{-2}]	$\overline{CF_{low}}$*	$\overline{F_{mix}}$	$\overline{F_{liq}}$	F_{seed}	LWP_{low}	IWP_{low}	$\overline{T_{ct}}$ [°C]	$\overline{H_{ct}}$ [km]
obs	199.2	0.82	0.53	0.47	–	–	–	-11.3	1.77
DYAMOND with convection									
DYA-80-conv	10.1	-0.37	0.86	0.14	0.22	55	–	-7.8	1.55
DYA-40-conv	7.0	-0.35	0.85	0.15	0.20	68	–	-7.8	1.57
DYA-20-conv	6.4	-0.36	0.83	0.17	0.20	73	–	-7.6	1.57
DYAMOND without convection									
DYA-80	-4.1	-0.23	0.88	0.12	0.19	75	–	-9.0	1.54
DYA-40	-7.9	-0.15	0.87	0.13	0.17	91	–	-9.2	1.52
DYA-20	-5.2	-0.19	0.87	0.13	0.17	88	–	-9.0	1.50
DYA-10	-3.9	-0.22	0.82	0.18	0.17	98	–	-8.7	1.55
DYA-5	-0.9	-0.28	0.81	0.19	0.18	88	–	-8.6	1.55
DYA-2.5 1.6	-0.32		0.78	0.22	0.18	84	–	-8.6	1.57
Additional Sensitivity Experiments									
EXP-80	-4.1	-0.23	0.77	0.23	0.28	62	94	-9.8	1.75
EXP-80-conv	5.3	-0.32	0.77	0.23	0.24	50	79	-8.6	1.72
EXP-80-convExp	5.8	-0.32	0.76	0.24	0.20	50	78	-8.6	1.71
EXP-80-conv-2.5Dt	4.5	-0.29	0.80	0.2	0.25	59	83	-8.7	1.72
EXP-20-conv	4.4	-0.34	0.77	0.23	0.20	59	91	-8.4	1.69
EXP-80-conv-20Dt	5.2	-0.30	0.79	0.21	0.23	55	75	-8.6	1.73
EXP-80-conv-Ised	4.5	-0.32	0.77	0.23	0.24	49	84	-8.4	1.71

LIST OF FIGURES

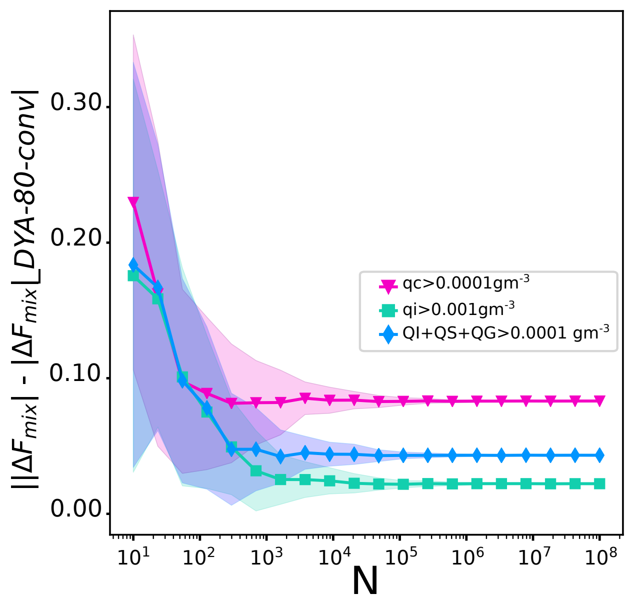

FIG. 1. Absolute mean difference of the simulated mixed-phase occurrence fraction bias ΔF_{mix} (defined in section 2) diagnosed using three alternative cut-off thresholds for time-averaged (small letters) or instantaneous (capital letters) ice-phase and liquid water contents. Differences are computed relative to ΔF_{mix} diagnosed for DYA-80-conv simulation using $qc > 10^{-2}$ g m^{-3} and $qi > 10^{-4}$ g m^{-3}. Bias of each simulation is computed with respect to F_{mix} diagnosed from DARDAR-v2.

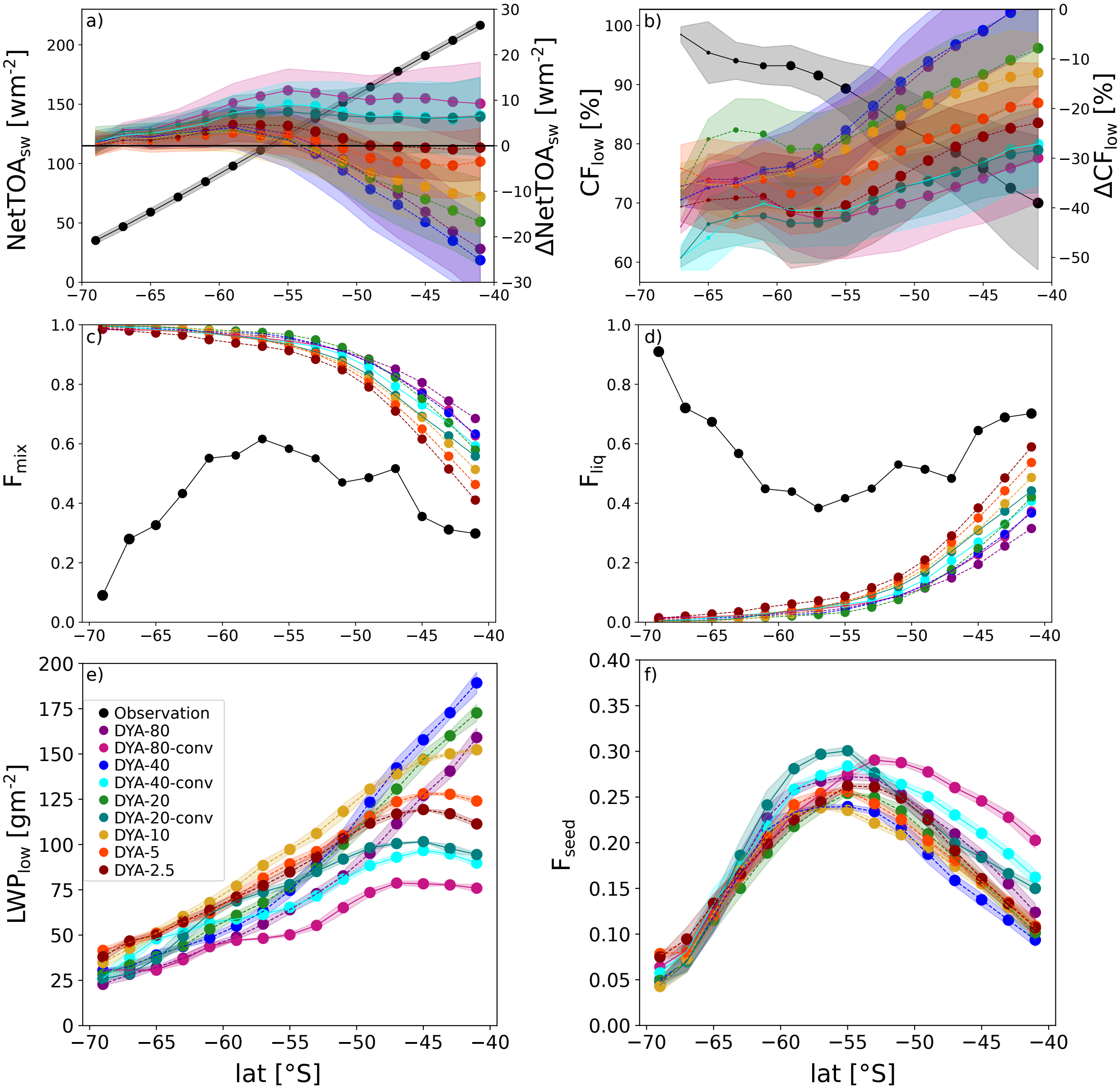

FIG. 2. Zonal mean cross sections of all DYA experiments for a) the bias in top-of-atmosphere net shortwave radiation ($\Delta NetTOA_{sw}$), b) the absolute cloud fraction bias (ΔCF_{low}), the normalised occurrence rate of c) mixed-phase clouds (F_{mix}) and d) liquid clouds (F_{liq}), e) low-cloud liquid water path (LWP_{low}) and f) seeding frequency F_{seed}. The data is binned in 2° latitude bins. Both solar insolation (as expected in austral summer) and number of cloudy points (CF_{low} computed on $1° \times 1°$ grid) decrease poleward. The shading denotes the spatial spread (standard deviation) within each latitude bin. Panels a) – c) include the following observations respectively: CERES $NetTOA_{sw}$, MODIS CF_{low}, DARDAR-v2 F_{mix} and F_{liq}.

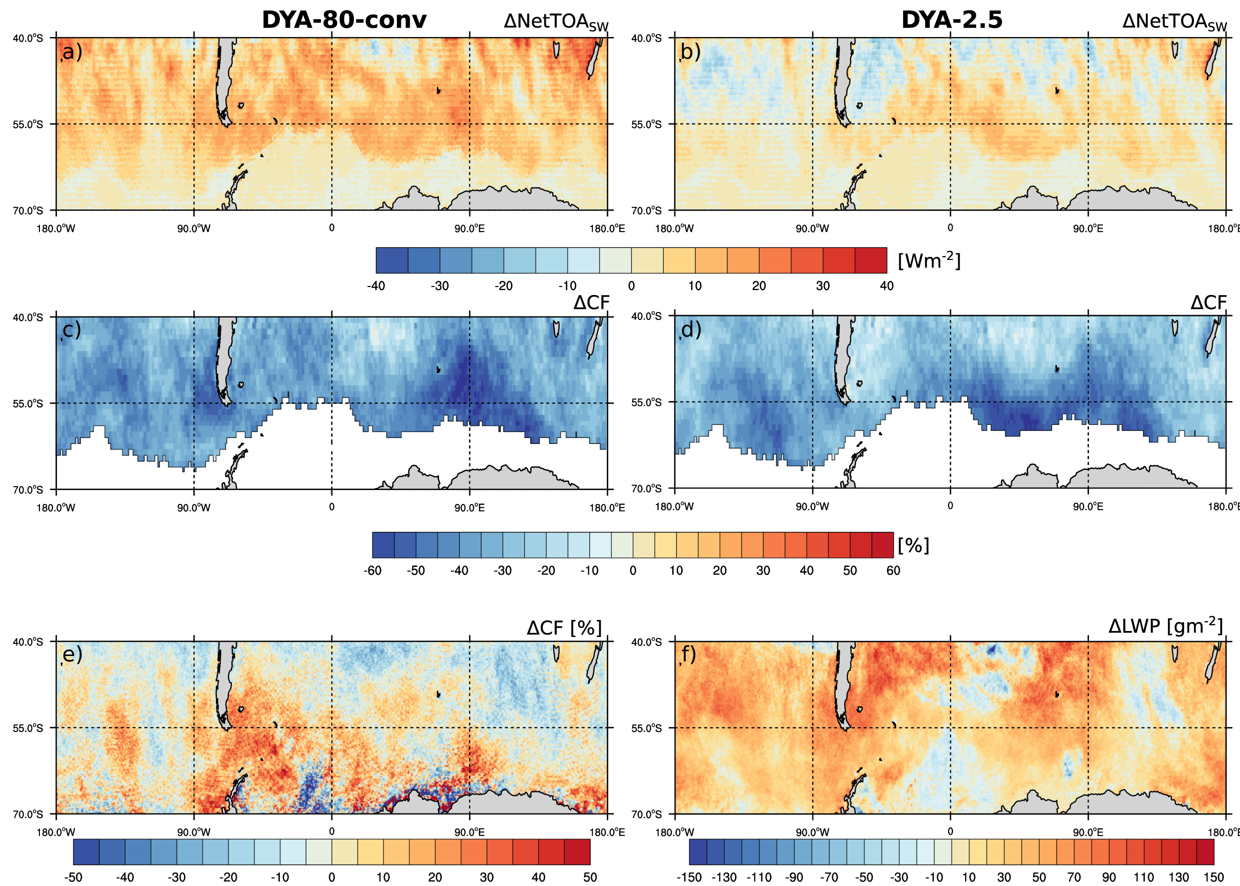

FIG. 3. Bias in a,b) monthly mean net all-sky *+ve* downward top-of-atmosphere shortwave radiation bias ($\Delta NetTOA_{sw}$) with respect to CERES retrieval for August 2016, and c,d) low-level cloud fraction over ocean surface bias ΔCF_{low} with respect to MODIS low (pressure > 680 hPa) cloud fraction. Results are shown for DYA-80-conv (LHS) and DYA-2.5 (RHS). e,f) show difference maps between both simulations (DYA-2.5 - DYA-80-conv) for CF_{low} and LWP_{low} respectively.

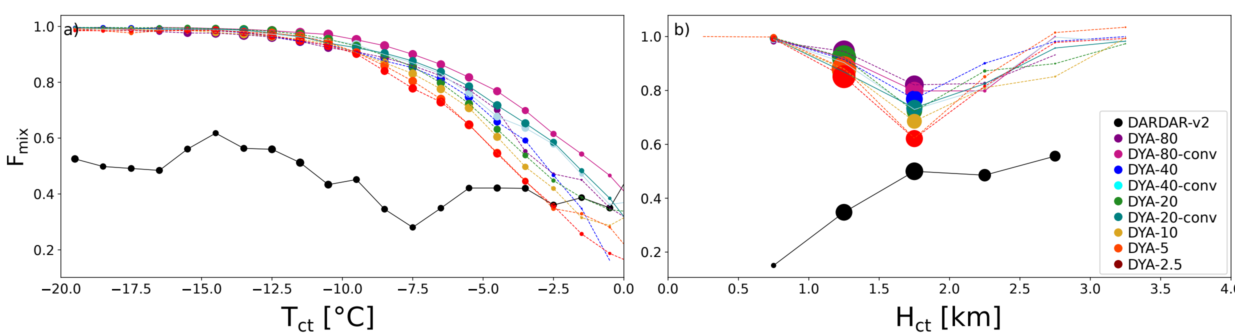

FIG. 4. Normalised mixed-phase occurrence rate (F_{mix}) against (a) cloud-top temperature (T_{ct}) and b) cloud-top height (H_{ct}). DYA experiments across all resolutions overestimate F_{mix} for $T_{ct} < -5\,°C$ and for all H_{ct}. The marker size scales with the relative occurrence of SO datapoints from August 2016 within each bin (bin-widths: a) 1 °C and b) 500 m).

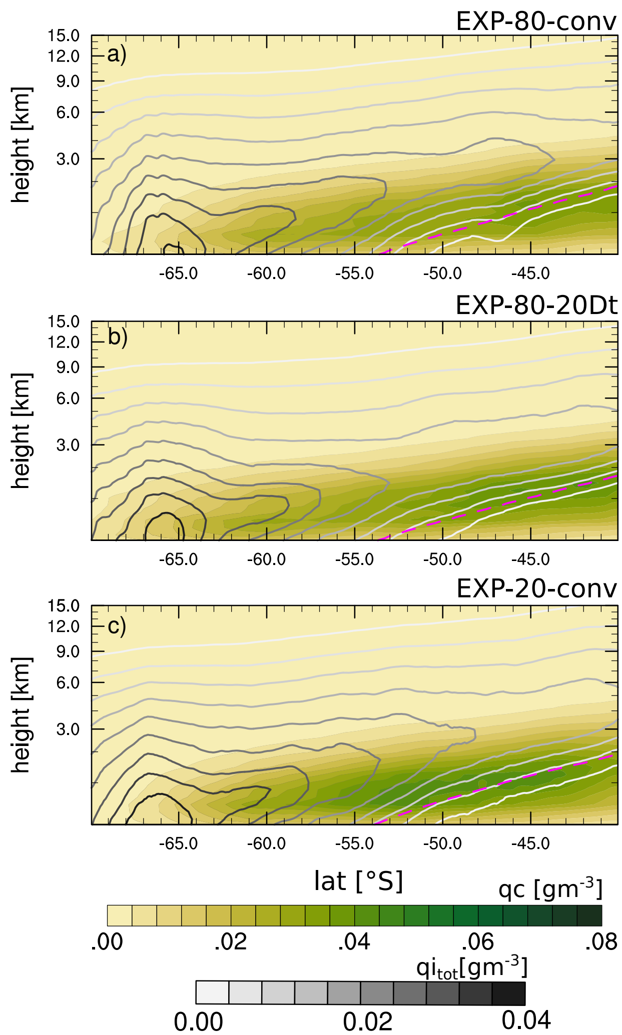

FIG. 5. Cross sections of zonal and monthly mean cloud water content (qc) total ice water content (qi_{tot} = $qi+qs+qg$) for August 2016. Magenta line denotes the zonal and monthly mean freezing line.

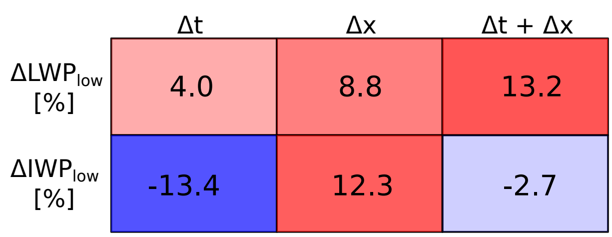

FIG. 6. Schematic summarising the relative change in low-level mixed-phase cloud liquid water path (LWP_{low}) and total ice water path (IWP_{low}) north of $-63°$ for a change in temporal and spatial resolutions separately as well as the combined impact.

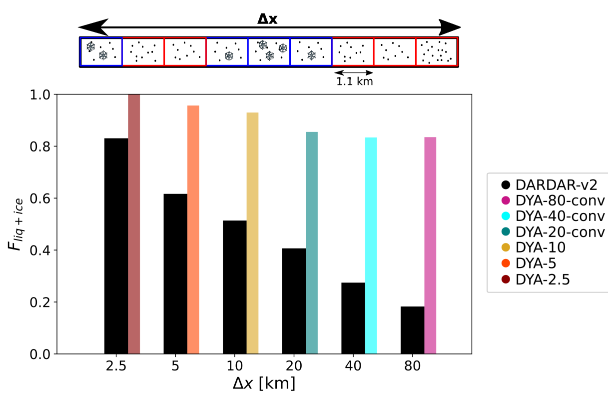

FIG. 7. Average fraction of points of coexistent liquid and ice in continuous liquid containing cloud segment of length Δx in the SO. $F_{liq+ice}$ is diagnosed along the combined CALIPSO and CloudSat track with a footprint of 1.1 km (black). The same analysis has been done for the fraction of mixed-phase 2.5km segments across all ICON resolutions (i.e. $F_{liq+ice} = 1$ by definition for DYA-2.5).